JOURNAL OF SPACECRAFT AND ROCKETS
Vol. 53, No. 4, July-August 2016

Global Aeroheating Measurements of Shock–Shock Interactions on Swept Cylinder

Michelle L. Mason* and Scott A. Berry†
NASA Langley Research Center, Hampton, Virginia 23681

DOI: 10.2514/1.A33434

The effects of the fin leading-edge radius and sweep angle on peak heating rates due to shock–shock interactions were investigated in the NASA Langley Research Center 20-Inch Mach 6 Air Tunnel. The cylindrical leading-edge models, with radii varied from 0.25 to 0.75 in., represent wings or struts on hypersonic vehicles. A planar oblique shock at 16.7 deg to the flow intersected the fin bow shock, producing a shock–shock interaction that impinged on the fin leading edge. Three fin sweep angles were tested: 0, −15, and −25 deg (swept forward). Global temperature data were obtained from the surface of the fused silica fins using phosphor thermography. Metal oil-flow models were used to visualize the streamline patterns for each angle of attack. High-speed zoom-schlieren videos were recorded to show the features of the shock–shock interactions. The temperature data were analyzed using one-dimensional semi-infinite and one- and two-dimensional finite-volume methods. These results were compared to determine the proper heat transfer analysis approach to minimize errors from lateral heat conduction. The dimensional peak heat transfer coefficient augmentation increased with decreasing leading-edge radius. The dimensional peak heat transfer output from the two-dimensional code was about 20% higher than the value from a standard, semi-infinite one-dimensional method.

Nomenclature

A	=	area, ft^2
c_h	=	convective heat transfer coefficient, $lb_m/(ft^2 \cdot s)$
c_P	=	specific heat capacity at constant pressure, $Btu/(lb_m \cdot °R)$
h	=	enthalpy, Btu/lb_m
k	=	thermal conductivity, $Btu/(h \cdot ft \cdot °R)$
L	=	full length of model leading edge, in.
M	=	Mach number
n	=	number of time steps in finite-volume algorithm, or cells in radial (nr) and lateral (nz) directions
P	=	pressure, psia
$\dot{q}$	=	heat transfer rate, Btu/h
R	=	radius of model, in.
r	=	radial direction in cylindrical coordinates
Re	=	unit Reynolds number, 1/ft
T	=	temperature, °R
t	=	time, s
U	=	velocity, fps
V	=	volume, ft^3
x, z	=	lateral direction in the Imaging for Hypersonic Experimental Aeroheating Testing program (x) or in cylindrical coordinates (z)
ε	=	emissivity of phosphor-coated fused silica models
ρ	=	density, lb_m/ft^3
σ	=	Stefan–Boltzmann constant, $Btu/(h \cdot ft^2 \cdot °R^4)$

Subscripts

aw	=	adiabatic wall
cond	=	conduction
conv	=	convection
d	=	known conditions at model surface
FR	=	Fay–Riddell
rad	=	radiation
ref	=	reference from mean baseline heating
t, 1	=	reservoir stagnation
tw	=	tunnel wall
w	=	wall (surface of model)
∞	=	freestream conditions

Presented as Paper 2015-3109 at the 45th Thermophysics Conference, Dallas, TX, 22–26 June 2015; received 17 September 2015; revision received 15 January 2016; accepted for publication 14 March 2016; published online 12 July 2016.

*Aerospace Engineer, Aerothermodynamics Branch, MS 408A. Member AIAA.

†Aerospace Engineer, Aerothermodynamics Branch, MS 408A. Associate Fellow AIAA.

I. Introduction

COMMERCIAL, government, and military applications rely on research into safe, reliable hypersonic technology. Vehicles designed to fly at hypersonic speeds, such as the now-retired Space Shuttle Orbiter and either planes or missiles with integrated ramjet or supersonic combustion ramjet (scramjet) engines, can be subjected to a phenomenon called a shock–shock interaction that causes significant, localized surface temperature and pressure augmentations [1,2]. Interactions between the vehicle's bow shock and the shock around the leading edge of a strut or a wing can compromise the vehicle's structural components in the absence of protective measures. Numerous experiments have investigated shock–shock interaction behavior and the resulting heating effects that occur in the hypersonic flight regime to aid in the development of thermal protection systems [3–10]. These studies classified shock–shock interaction types and pointed to the need for improved spatial resolution of the data in the regions affected by the interactions as well as the potential need to add two-dimensional (2D) heat transfer analyses to the standard one-dimensional (1D) techniques if a strong lateral temperature gradient exists. Measurement techniques have gradually improved to provide better spatial resolution in shock–shock interaction heat transfer analyses.

Shock–shock interactions in hypersonic flow, as described in this study, involve an oblique incident shock generated by a flat plate shock generator (SG) that intersects a bow shock around a blunt body. Edney [1] identified six general types of interactions between bow shocks around blunt bodies and incident shocks. The relative angle between the incident shock and the bow shock as well as the strengths of these two shocks dictate the features of the resulting shock impingement, such as the angle of the reflected shock, the number of shear layers that form, and the presence of a supersonic jet. These shock–shock interactions are sketched in Fig. 1. Of the six types Edney described, the type III and IV interactions are likely to produce the worst heating to the vehicle since the shear layer or jet impinges directly on the surface. Since the time of Edney's study, another

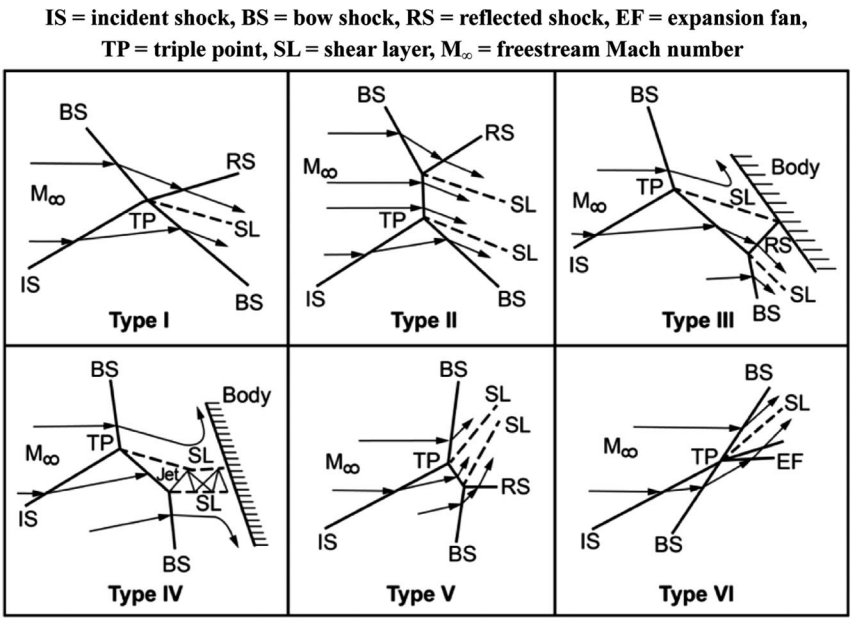

a) Six classic shock interaction types as classified by Edney [1]

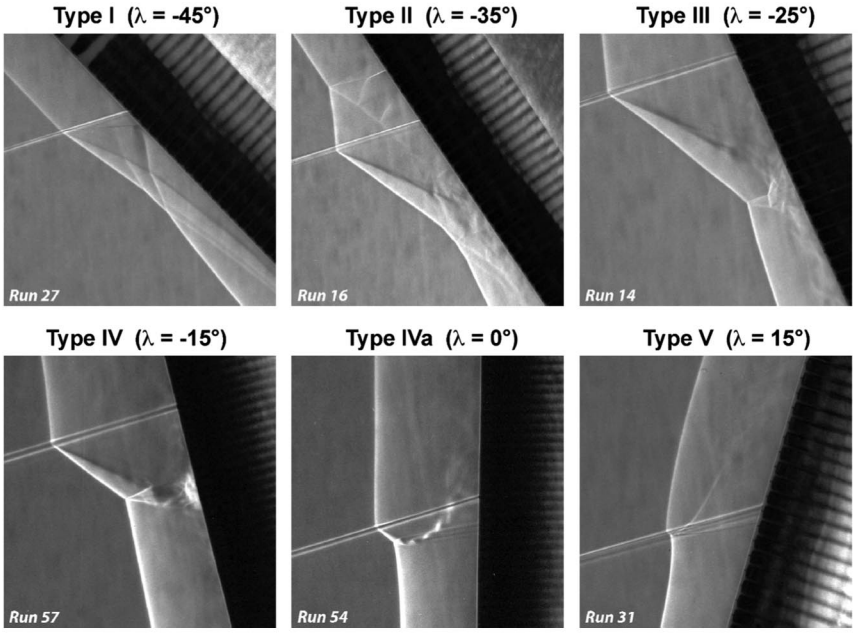

b) Photographic examples of these shock interaction types taken during test 6692 [11]

Fig. 1 Shock interaction types.

subtype has been added to the shock–shock interaction lexicon, the type IVa interaction, in which the supersonic jet is present but largely misses the surface of the body.

Berry and Nowak [11] experimentally investigated the effect of the fin sweep angle on the increase in the peak heating on a leading edge or strut of a hypersonic vehicle due to different types of three-dimensional (3D) shock–shock interactions. The study in [11] included a systematic sweep of fin angles to capture most of the general classification types, as shown in the schlieren images in Fig. 1. Temperatures measured using Macor® models instrumented with thin-film gauges were reduced using a 1D heat transfer code. Berry and Nowak postulated that the nondimensional peak heating increase for a type IV interaction (on a 0.25-in.-radius model) might grow from nearly seven times the baseline value (defined in [11] as heating in the absence of a shock–shock interaction) to a factor of 10 if lateral conduction effects were considered in the heat transfer analysis. The peak heating increase for a type III interaction was, again, nearly seven times the baseline value. Most of the wind tunnel runs in [11] were conducted at a unit Reynolds number (Re_∞) of 2.1×10^6/ft with the SG at 9 deg to the flow. The results of [11] were used to select a smaller subset of fin angles to investigate in the present study.

Wright et al. [12] conducted numerical simulations using the General Aerodynamic Simulation Program and the Data Parallel

Table 1 Actual mean flow conditions in Tests 6976 and 6983 in the 20-Inch Mach 6 Air Tunnel

M_∞	Re_∞, ft^{-1} $\times 10^6$	$P_{t,1}$, psia	$T_{t,1}$, °R	ρ_∞, $\times 10^{-4}$ slug/ft^3	T_∞, °R	U_∞, fps
5.90	1.1	60.5	875.1	0.33	110.3	3035
5.96	2.1	125.5	898.5	0.63	111.3	3082
6.00	4.1	252.2	901.6	1.23	110.5	3087

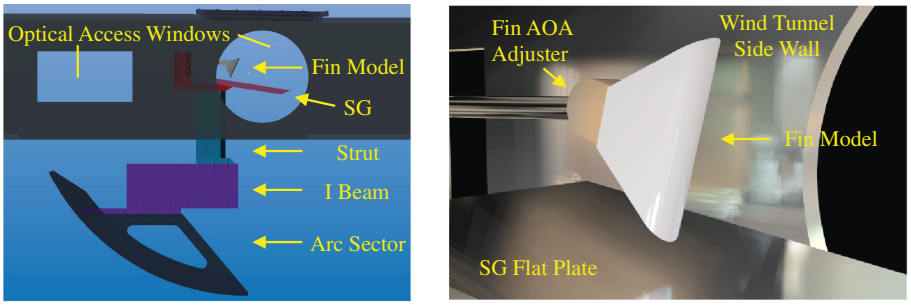

a) Model/tunnel hardware b) Close-up of the fin at –15° AOA

Fig. 2 CAD mockup in the tunnel to verify optical access to the fin (flow right to left).

Line Relaxation computational fluid dynamics (CFD) codes for a model geometry and flow conditions similar to the Berry and Nowak [11] study. Wright et al. found that circumferential heat flux gradients are an order of magnitude smaller than the longitudinal gradients along the leading edge of the model. These CFD simulations predicted a peak augmentation of 8 for the type IV interaction, 6.5 for the type III interaction, and only 1.6 times the baseline value for the glancing type IV interaction.

Walker and Scott [13] developed 1D and 2D inverse conduction codes to estimate the heat flux from a shock–shock interaction to the fin model in the Berry and Nowak [11] study. These codes were used to determine the effect of lateral conduction on the heat flux in regions with severe temperature gradients. Walker and Scott used the thin-film-gauge data from [11] as inputs to the conduction codes for sample cases with the Macor and Upilex® models. The results from the 2D code for the Macor model reveal a difference of ±20% at the heat flux peaks and valleys compared to the results from a 1D code with the same temperature inputs. The heat flux values in the regions outside of the peak (where the temperature gradient between neighboring gauges is smaller) are very similar between the 1D and 2D codes since both algorithms assume flat plate geometries. Walker and Scott also concluded that the heat flux calculations could be improved by increasing the spatial resolution of the acquired temperature data.

This research is the first known published study in which global thermal imaging techniques are used in conjunction with multi-dimensional thermal analyses to investigate high heating rates associated with shock–shock interactions. The phosphor thermography technique provides temperature and heat transfer data with an increased spatial resolution compared to the discrete sensors typically used in prior shock–shock interaction studies. Additionally, the current study provides information about shock–shock interactions from improved experimental tools such as high-speed zoom-schlieren and two separate oil-flow techniques.

II. Facility

The facility used for the present study was the 20-Inch Mach 6 Air Tunnel in the Langley Aerothermodynamics Laboratory at NASA Langley Research Center (LaRC) [14]. This perfect gas facility has well-characterized flow uniformity and composition [15]. The tunnel reservoir stagnation pressure and temperature, $P_{t,1}$ and $T_{t,1}$, are accurate to within ±2%. The LaRC 20-Inch Mach 6 Air Tunnel is a blowdown wind tunnel. Dry air from two high-pressure bottle fields is transferred to a 600 psia reservoir, where an electrical resistance heater heats the air to a maximum temperature of 1000 °R. The flow passes through two filters rated for 10 μm (3.94×10^{-4} in.) and 5 μm (1.97×10^{-4} in.) particles, respectively, that are installed between the heater and the settling chamber before entering the 20.5×20 in. test section at Mach 6. The top and bottom walls of the 2D nozzle are contoured, and the side walls are parallel. This wind tunnel exhausts into combined 41- and 60-ft-diam vacuum spheres, a 100-ft-diam vacuum sphere, or to the atmosphere through an annular steam ejector. Freestream flows with Mach numbers between 5.8 and 6.1 and unit Re_∞ numbers between 0.5×10^6/ft and 8.3×10^6/ft are possible in this facility [16].

Models are typically mounted on the arc-sector injection system located in a housing below the test section. This injection system is used to quickly insert the model into the flow after the tunnel has been started. Aeroheating tests generally have total run times of 30 s, with typical model injection times of approximately 1.5 s and a model residence time on the tunnel centerline of approximately 5–10 s. The actual mean flow conditions for this study are provided in Table 1. These flow conditions were calculated by averaging the parameters for 30 runs at a unit $Re_\infty = 2.1 \times 10^6$/ft and two runs at a unit $Re_\infty = 1.1 \times 10^6$/ft. The parameters for a unit $Re_\infty = 4.1 \times 10^6$/ft correspond to the one run that was conducted at that unit Re_∞ number.

III. Experimental Setup

Figure 2 shows a graphical representation of the test hardware used for this study. The key components in Fig. 2 are the SG, a flat plate with a sharp leading edge that produces a 16.7 deg planar incident shock at Mach 6, and the model, inclined at −15 deg in the figure. Similar images of these computer-aided design (CAD) models were used before the test to ensure the visibility of the leading edge through the wind tunnel windows for each configuration. In each case, the upper tip of the model was swept 0, 15, or 25 deg forward of vertical, defined as 0, −15, and −25 deg model angles of attack (AOA), respectively. Figure 2a also shows the arc sector positioned below the test section in the 20-Inch Mach 6 Air Tunnel. Ten bolts (five on each side) secured an I beam to the arc sector using a 1-in.-thick spacer to center the model in the core flow of the wind tunnel. Three bolts on either side secured the strut to the I beam. The strut head plate was bolted to the top surface of the strut to support the stainless steel SG (6 in. wide by 17 in. long) angled 9 deg from horizontal. A stainless steel support that allows height adjustments was bolted into the strut head plate behind the SG. This support held the model above the SG using a 0.5-in.-diam sting. The model was bolted to the sting through a component used to change the AOA of the model, called the fin AOA adjuster.

In Fig. 3, the model support system is retracted into the box below the tunnel test section. A single thermocouple was embedded at the

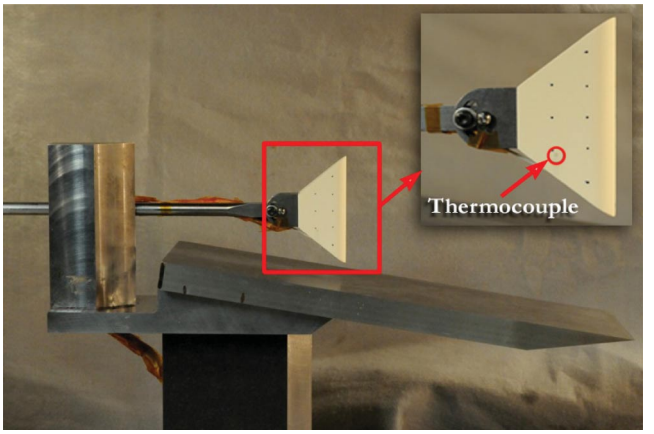

Fig. 3 Photograph of the installed model that indicates the thermocouple location on the ceramic fin.

surface of each fused silica model just below the phosphor coating. The bead location for the 0.5-in.-radius model is labeled in the figure. These thermocouples measured the change in temperatures between the time the pre-run phosphor thermography image was recorded and the time that the run began to determine the proper offset for the leading-edge, pre-run temperatures input to the 1D and 2D finite-volume (FV) codes in the heat transfer analyses. The stainless steel fin AOA adjuster is shown more clearly in the inset image. A hinge pin with a retaining ring allowed the model to be rotated through any AOA between −45 and 45 deg from horizontal. An inclinometer was used to set the AOA of the fin. The model was always positioned between 0.5 and 0.75 in. above the flat plate SG or the strut head plate to eliminate interactions between the tip of the model and the flat plate boundary-layer (BL) flow. Flow density gradients behind the models and shock–BL interactions with the flow over the SG are discussed more in [17].

Oil-flow and schlieren data were collected to visualize surface streamlines and flow density gradients, respectively, in the vicinity of the off-surface shock–shock interactions to provide insight into the flow behavior. The surfaces of stainless steel models, cut by a wire electrical discharge machine, were polished smooth and covered with multiple layers of high-temperature flat black paint (heat resistant up to 1200 °F). This coating provided sufficient contrast with a white-pigmented oil in videos and images during and after the oil-flow wind tunnel runs. Two oil-flow techniques were used. In the first method, a clear base coat of 350 cs oil was applied to the model, and dots of 350 cs oil mixed with a titanium white pigment were flicked onto the model surface. During the run, these dots merged into streaks of oil along the flow streamlines. For the second method, the model was uniformly covered with a full layer of 350 cs oil mixed with pigment to reveal regions of high or low shear on the model. The flow density gradients were recorded with a custom zoom-schlieren system that used a set of lenses with a continuous light source to magnify a smaller region of interest encapsulating the shock–shock interaction in the flow. More details about the oil-flow and schlieren techniques are provided in [17].

The mostly solid, porous fused silica models facilitated a 2D conduction assumption through a half cylinder to represent the model leading edge in the FV heat transfer codes. These models were covered with a phosphor mixture composed of ZnCdS:Ag,Ni and $La_2O_2S:Eu^{3+}$. These components work together as a two-color relative intensity phosphor coating that is sensitive to temperature changes on the surface of a wind tunnel model. Fiducial marks are dots applied to a model in specified locations that are used to correlate distances between features in an image to the physical dimensions of the model. Fiducial marks were applied to the oil-flow models (using orange fluorescent enamel paint) and the phosphor-coated models (using blue ink [18]) in the same pattern for all the models that shared the same nose radius. The model fabrication process is further discussed in [17].

Phosphor thermography was implemented to obtain a temporal record of surface temperatures for the models during the wind tunnel runs. Merski discusses a data reduction program called Imaging for Hypersonic Experimental Aeroheating Testing (IHEAT) used to obtain quantitative wind tunnel aeroheating data [19,20]. This phosphor thermography method is routinely used to determine the global surface heating distribution on hypersonic wind tunnel models. In the heating cases without a shock–shock interaction, the phosphor thermography images were recorded at 10 fps after the initial images were taken when the model reached the wind tunnel centerline. During the runs with a shock–shock interaction, the phosphor data were acquired at 30 fps to maximize the amount of data obtained before the leading-edge temperatures exceeded the maximum phosphor system limit, which is approximately 320 °F. The thermocouple data were obtained at 30 Hz. Between wind tunnel runs, the ceramic model was allowed sufficient time to cool down to room temperature conditions.

Figures 4a–4c show the marked models, including the backup (left side) and primary (middle) fused silica models and the metal oil-flow models (right side). The images in Figs. 4d and 4e show the 0.75-in.-radius metal model (top image), without a coating of oil, and the 0.50-in.-radius fused silica model (bottom image) in the tunnel test section. These models are illuminated with ultraviolet light to reveal the fluorescent fiducial marks and the phosphor coating, respectively.

The 20-Inch Mach 6 Air Tunnel runs were conducted either without a SG installed or with a 9 deg SG angle. For most of these runs, the nominal Mach number was 5.96, and the unit Re_∞ number was 2.1×10^6/ft. A unit Re_∞ number sweep was conducted with two runs at 1.1×10^6/ft, one run at 2.1×10^6/ft, and one run at 4.1×10^6/ft for the 0.25-in.-radius model at a −15 deg AOA. The model AOA was either 0, −15, or −25 deg in each case to yield a type IVa, a type IV, or a type III interaction. These shock–shock interaction types were visually confirmed using high-speed schlieren data obtained with a Phantom 9 (1600 fps) and a Phantom 12 (7900 fps) camera. Phosphor thermography data were first obtained with the

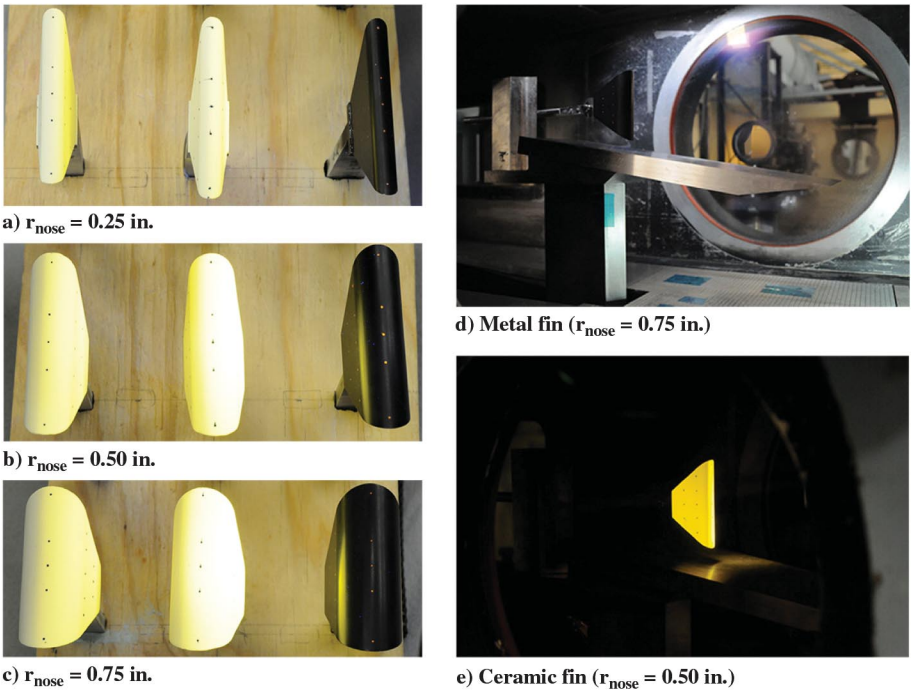

Fig. 4 Models available for the current study with a range of nose radii.

entire fin leading edge in the field of view (referred to as zoomed out) and in a separate run with the camera focused on the region of interest (or zoomed in). The second run was performed to maximize the spatial resolution of the acquired data in the shock–shock interaction region. Additional information about the data acquisition processes and the run matrix is provided in [17].

IV. Heat Transfer Analysis

Surface heat transfer coefficients based on the temperature readings for the fused silica models were calculated using IHEAT and 1D and 2D FV conduction codes. These programs were used to determine the optimum method to predict heating profiles if models were exposed to sharp temperature gradients, which in this study were produced by shock–shock interactions. The IHEAT code is the method used to analyze phosphor thermography data obtained in Langley's hypersonic facilities. IHEAT is a 1D code that assumes the model is semi-infinite in the through-thickness dimension, so heat applied at the surface does not reach the back of the model during a short wind tunnel run. Convective heat transfer coefficients c_h are calculated from a convective heat transfer $\dot{q}_{\text{conv}}$ equation based on an enthalpy difference, i.e.,

$$\dot{q}_{\text{conv}} = c_h(h_{\text{aw}} - h_w) \tag{1}$$

Additional assumptions and equations incorporated in the IHEAT code are described in [19,20].

Two direct, finite-volume codes were written in Fortran to approximate the conduction in the phosphor-coated fused silica models. The 1D code assumed heat was conducted only through the thickness of the model, while the 2D code also considered conduction in the direction parallel to the leading edge. The purpose of the 1D FV code in the present study was to provide a direct comparison between the 1D algorithm in IHEAT and the assumptions in the FV codes for the 1D vs 2D comparison. Both the IHEAT and 1D FV codes neglect the effect of surface curvature.

The diagram in Fig. 5 shows the cylindrical geometry used in the 2D code to approximate the model leading edge. To simplify the calculations, the code assumes a cylinder with dimensions equal to the leading-edge length of 4 in. and the appropriate nose radius. A rectangle bounded by the stagnation line on the leading edge and the centerline of the cylinder (in red in Fig. 5) defines the boundaries of the nodes in both FV codes. The 2D code used cylindrical cell volumes that surrounded nodes in the rectangular plane. Definitions of the areas and volumes around the nodes in the 2D grid as well as the number of volumes and the corresponding spacing in the radial and lateral directions are provided in [17]. The coordinate systems in the figure apply to both FV codes.

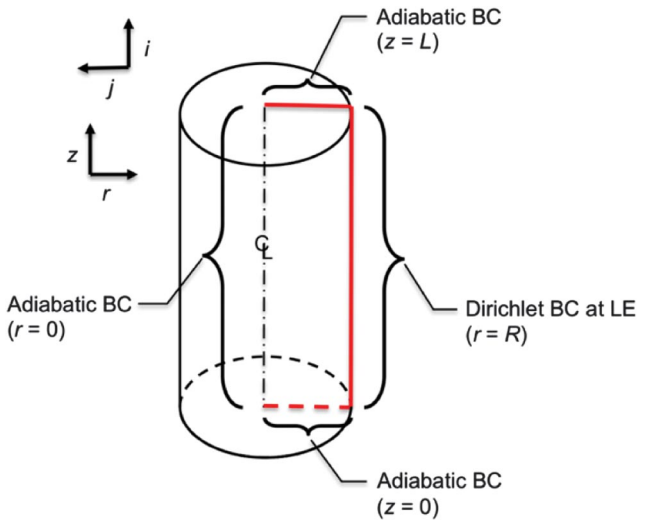

Fig. 5 Boundary conditions (BC) of the fin cylindrical leading edge (LE) modeled in 1D and 2D FV codes.

Two boundary conditions were applied to the grid of finite volumes in the 1D code, and four boundary conditions were applied in the 2D code. A Dirichlet boundary condition was applied at the surface ($r = R$) in both codes using the known temperatures T_d of the models at each time step. An adiabatic boundary condition (no heat transfer) was assumed at the cylinder centerline ($r = 0$) in both codes. The boundary conditions at the top ($z = L$) and at the bottom ($z = 0$) of the cylinder in the lateral direction were also adiabatic in the 2D code. Adiabatic boundaries were assumed because temperature data were not available for nodes outside of the rectangular plane. Thus, the discrete heat transfer expressions that included nodal information external to the boundary nodes were assumed to be equal to zero. This assumption affected the data computed at the tips of the model but did not significantly alter the data in the region of the shock–shock interaction, which is the focus of this study.

The 1D code used a FV formulation of the Crank–Nicolson algorithm to solve the discretized conduction equation in the radial direction. The Crank–Nicolson method employs the trapezoidal rule of time integration in which the discrete spatial temperature gradient is evaluated as an average of the gradient at the current (n) and future ($n + 1$) time steps [21]. This method yielded an unconditionally stable time-marching scheme in the 1D FV code. The resulting system of equations formed a tridiagonal system matrix that was multiplied by the temperatures at the central nodes of each cell. These equations comprised a system matrix used in the implicit Thomas Algorithm [22] to solve for the nodal temperatures.

The 2D conduction equation was discretized using a FV, unconditionally stable, alternating direction implicit (ADI) algorithm [22]. This method sweeps through the geometry of the model twice for every time step: first in the z direction (along the fin leading edge) for all the nodes and then in the r direction (radially) using an updated temperature distribution T^* at the intermediate time step ($\Delta t/2$). Chapter 4 in [17] describes the equations used to calculate an initial temperature distribution in the 1D and 2D codes. The heat transfer coefficients were calculated at the end of each full time step in both the 1D and 2D FV codes. An energy balance between the stored heat and the radiation, convection, and 2D conduction heat transfer at the model surface is given by

$$\rho c_P V\frac{\partial T}{\partial t} = \frac{\partial}{\partial r}\left(A_{\text{cond}}k\frac{\partial T}{\partial r}\right) + \frac{\partial}{\partial z}\left(A_{\text{cond}}k\frac{\partial T}{\partial z}\right) - [A_{\text{rad}}\varepsilon\sigma(T_{i,j}^4 - T_{\text{tw}}^4)] - A_{\text{conv}}c_h(h_{\text{aw}} - h_w) \tag{2}$$

The variables A_{cond}, A_{rad}, and A_{conv} represent the areas through which heat is transferred by conduction, radiation, and convection, respectively. These variables varied depending on the volume V of the cell for which the heat transfer was computed. The variable ε is the emissivity, σ is the Stefan–Boltzmann constant, T is the temperature at a given location (either at each node specified by i in the 1D code or i, j in the 2D code or at the tunnel wall tw), h_{aw} is the adiabatic wall enthalpy, and h_w is the enthalpy of the air at the surface temperature of the model. The density ρ, specific heat c_P, and thermal conductivity k in the heat transfer equation are shown as constant values. In both the 1D and 2D FV conduction codes, the thermal properties of c_P and k depended on temperature and were updated after each full time step. The left side of Eq. (2) represents energy stored in the object due to a temporal temperature gradient, $\partial T/\partial t$. The right side represents heat conducted through the object due to a second-order spatial temperature gradient, either $\partial^2 T/\partial r^2$ or $\partial^2 T/\partial z^2$. After the heat transfer equation was properly discretized, the equation was rearranged to solve for the enthalpy-based heat transfer coefficient c_h for each surface volume at a nondimensional position specified as the spatial location x (which is equal to zero at the lower tip) divided by the full length L (4 in.) of the leading edge, as shown in Fig. 6a for a 0.25-in.-radius model at a 0 deg AOA.

The FV codes computed a dimensional heat transfer coefficient based on the temperature data at each pixel along the leading edge of the model. The 1D code looped through input data to derive a heat

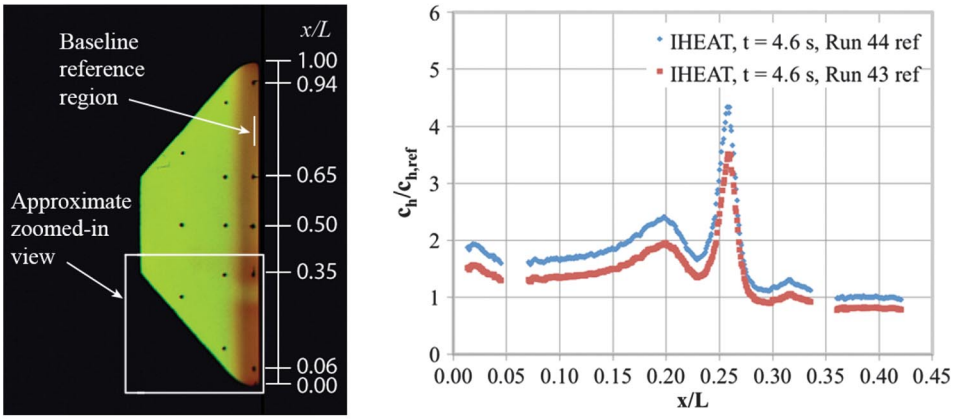

a) Fiducial mark scale on type IVa image **b) Heat transfer for zoomed-in type IV case (run 44)**

Fig. 6 Examples of a) heat transfer image and b) extracted line cut along the fin leading edge.

transfer coefficient at every pixel individually, while the 2D code calculated the data for the full leading edge using a line implicit scheme. These heat transfer coefficients were then nondimensionalized to determine the relative magnitude of the peak heating in the shock-interaction region compared to the baseline heating (no interaction). The heat transfer coefficients at $x/L = 0.75$ to $x/L = 0.85$ along the leading edge (relative to the x/L locations in Fig. 6) were relatively far away from both the peak heating region and the leading-edge fiducial marks. In the runs for which the full leading edge was visible in the image, these coefficients were averaged to provide a reference coefficient to derive the nondimensional data.

For the wind tunnel runs in which the camera was zoomed in on the shock-interaction region, baseline heating data from the region $x/L = 0.75$ to 0.85 were not available. To be consistent, each zoomed-in run used the average baseline value from the corresponding zoomed-out run as a reference value to calculate nondimensional data. The wind tunnel flow conditions varied slightly between runs, so this assumption could yield lower nondimensional peak heat transfer coefficients in some of the zoomed-in cases, as evidenced by the cases in which data outside the shock-interaction region were available and were less than a nondimensional baseline value of 1.0. This assumption was necessary to compare the nondimensional data for higher (zoomed-in) and lower (zoomed-out) spatial resolutions.

A comparison in Fig. 6b demonstrates the potential error associated with reducing the zoomed-in leading-edge data by a reference heat transfer coefficient from a separate wind tunnel run. If an average of the zoomed-in heat transfer data from Run 44 (between $x/L = 0.38$ and $x/L = 0.41$) was used to obtain nondimensional heat transfer coefficients, the peak heat transfer coefficient $c_h/c_{h,\text{ref}}$ was 4.3. However, if the reference value from Run 43 (averaged over $x/L = 0.75$ to $x/L = 0.85$) was used, the peak $c_h/c_{h,\text{ref}}$ was only 3.5. If data in Run 44 in the region between $x/L = 0.75$ and $x/L = 0.85$ were available to be used for a reference, nondimensional data from this run likely would lie somewhere between the two curves in the plot, since the average heat transfer in the region from $x/L = 0.38$ to $x/L = 0.41$ was typically slightly lower (i.e., by a difference of 0.015 for Run 43) than in the $x/L = 0.75$ to $x/L = 0.85$ region.

V. Experimental Measurements and Results

The effect of the fin sweep angle and leading-edge radius on the shock-interaction patterns and resulting surface heating are presented by a comparison of zoom-schlieren, oil-flow, and heat transfer results. The specific fin sweep angles examined in the present study are 0, −15, and −25 deg, where the negative angle denotes the fin is swept forward from the base. The latter two sweep angles provide cases with strong lateral temperature gradients due to the type IV and type III shock–shock interactions, respectively, and the 0 deg sweep angle yields a lower heating case for a type IVa interaction with smaller lateral temperature gradients. These cases were selected to assess the need for a two-dimensional analysis method. Also, three model geometries were tested to determine how the features of each type of interaction change due to the leading-edge radius. The following discussion is a preface to the subsequent results and analysis.

In the 2D schlieren images, the planar incident shock is seen as a line. The incident shock does not impinge on the model but instead wraps around the bow shock. The extrapolated incident shock location described in the following images references the location where the incident shock would impinge on the leading edge in the absence of the bow shock. In computed schlieren images of the stagnation plane derived from computational results (not included here), the incident shock does not appear to continue through the bow shock [17]. Experimental zoom-schlieren data initially were obtained at a framing rate of 1600 fps. Additional images were obtained at 7900 fps and higher framing rates, but either the acquisition rate was too slow or the contrast in the images was too poor to resolve the unsteadiness observed in the 1600 fps data, so the schlieren images acquired at 1600 fps are presented.

The type III and type IV interactions provided peak heat transfers that rapidly exceeded the maximum phosphor thermography temperature limit. For that reason, only temperature images acquired about 0.2 s after the model reached the wind tunnel centerline (or at a time $t = 1.8$ s after the model injection sequence started) were used in the heat transfer analysis. In most cases, all the temperatures in these early line cuts were within the phosphor limits, permitting a comparison of the trends in the heat transfer coefficients due to each shock–shock interaction for the three leading-edge radii. A temporal collapse plot of the leading-edge line cuts and an analysis of the trends in heat transfer coefficients in specific surface locations over time were used to determine when to take the line cuts [17].

The x axis in the heat transfer plots shows the nondimensional x/L locations for the 0.25-in.-radius model (referred to as $x/L_{0.25}$). These locations are offset for the 0.50- and 0.75-in.-radius models to align the notable features of the line cuts (either the valley for the type IVa interaction or the peaks for the type III and type IV interactions). Gaps in the line cuts along the leading edge indicate the removal of fiducial mark data. Five fiducial mark locations were used to align the model vertically in the wind tunnel and to guarantee that at least two fiducial marks were visible when the camera was zoomed in on the interaction region.

Contour maps of the 1D Fay–Riddell [23] nondimensionalized heat transfer coefficients from IHEAT are presented at $t = 1.8$ s. The limits on the color bar scale in each contour map were set to 0 and 3 to ensure the main features of the heat transfer pattern were visible for every test configuration. The average baseline heating data in the region away from the shock–shock interaction during the wind tunnel run were used to determine the relative heating augmentation in the presence of an interaction for the heat transfer line cuts. Since different reference values were used to convert the heat transfer contour maps and the line cuts to nondimensional data, the y-axis

scale in the plots does not directly correlate to the color bar on the contour maps.

Uncertainties in the phosphor thermography data depend on the rise in the model surface temperatures. The following values of uncertainty are based on historical tests with a variety of types of models. On surfaces with a significant temperature rise (>70 °F), uncertainties in the computed heat transfer values are in the range of ±10%. For moderate temperature increases (20–30 °F), the total heat transfer uncertainties are roughly ±25%. More information on phosphor thermography uncertainties is found in [19,20]. Error bars are not included in the plots due to the density of the data in the line cuts.

The peak heat transfer coefficient in the shock–shock interaction region increases with increasing leading-edge radius in the nondimensional line cuts. This trend is the opposite from the peak behavior in dimensional line cuts. This reversal in the leading-edge radius effects occurs because the reference value used to convert the heat transfer coefficients to nondimensional values decreases as the leading-edge radius increases, which amplifies the peak heat transfer value for the larger model geometries. Nondimensional heat transfer line cuts are presented to estimate the peak heating augmentation relative to the expected heat transfer in the absence of a shock–shock interaction.

Most of the following data were captured at a unit $Re_\infty = 2.1 \times 10^6/\text{ft}$. However, for the FV comparisons near the end of this results section, data from runs with a unit $Re_\infty = 1.1 \times 10^6/\text{ft}$ were used to ensure more time steps of useful heating data were available before the phosphor limit was exceeded in the shock–shock interaction region.

A. Fin Sweep of 0 deg

Figure 7 displays schlieren images of the 0.25-, 0.50-, and 0.75-in.-radius models, from left to right, at a 0 deg AOA. The shock interaction is so close to the incident shock in Fig. 7a that the type IVa features are difficult to distinguish, though a close inspection reveals a very narrow supersonic jet with shear layers turned upward. The extrapolated incident shock is further separated from the supersonic jet and the curled-up shear layers for the 0.50-in.-radius model in Fig. 7b. The shear layers appear to attach to the surface of the model above the location where the incident shock wraps around the bow shock, which is similar to the behavior demonstrated in Fig. 1b.

The bow shock standoff distance is greatest for the 0.75-in.-radius model, so the features of the type IVa interaction are easier to identify for that model. A narrow supersonic jet extends nearly horizontally from the location where the bow shock is nearly vertical. The jet then turns upward, and the shear layers that bound the jet spread apart to impinge on the surface of the model. A pattern of triangles that comprise the shock train formed by reflected shocks is visible near the beginning of the supersonic jet. The horizontal feature behind this shock train is likely a 2D projection of 3D flow density gradients that wrap around the model. The shear layers curve up past the extrapolated incident shock line, as was noted in videos of the schlieren data and is faintly visible in Fig. 7.

Oil-flow images in Fig. 8 show characteristic streamlines and shear patterns for this type IVa interaction with the 0.75-in.-radius model. The features in these oil-flow images are similar to the streamline patterns observed on the 0.25- and 0.50-in.-radius models. Figure 8b indicates the oil movement for a model that was initially fully coated with oil, while the other images show streamlines on a model that was covered with dots of pigmented oil before the run. The oil-flow streamlines on the leading edge in Fig. 8 are fundamentally similar to the oil-flow streamlines in the region of the shock–shock interaction for a 0.5-in.-radius cylinder in [10].

A horizontal line around the circumference of the leading edge in the full-coating image indicates the attachment point of the upper shear layer that curls up from the supersonic jet. Streamlines travel

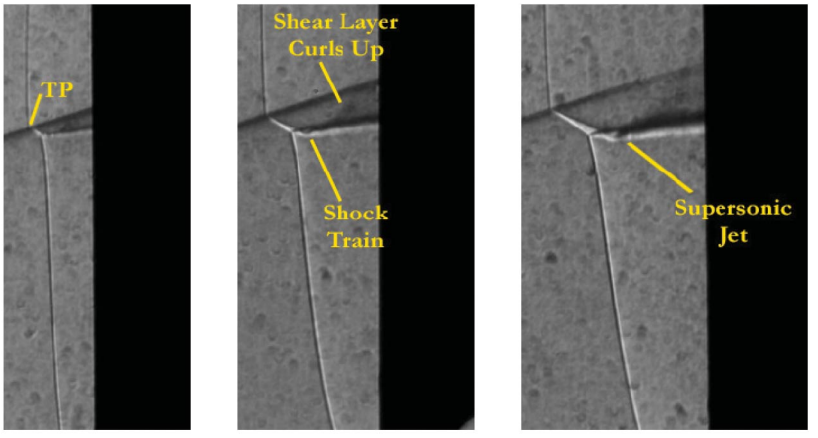

a) r_{nose} = 0.25 in. b) r_{nose} = 0.50 in. c) r_{nose} = 0.75 in.

Fig. 7 Type IVa interaction zoom-schlieren images (for 0 deg AOA and a unit $Re_\infty = 2.0 \times 10^6/\text{ft}$).

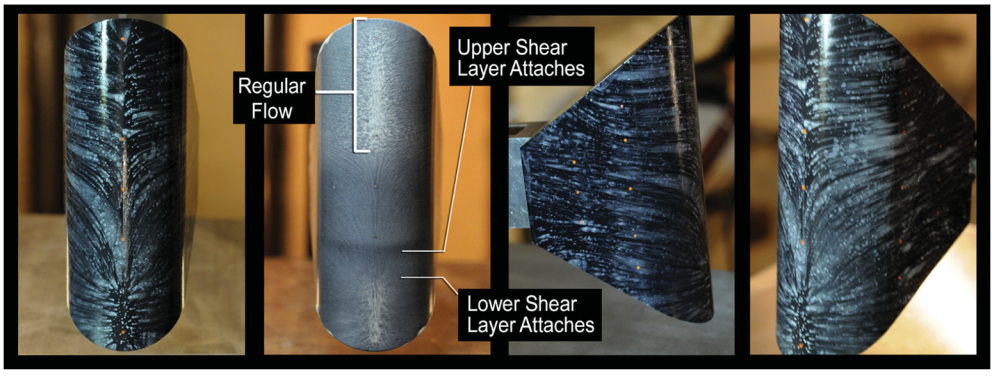

a) Dot technique b) Paint technique c) Dot technique d) Dot technique

Fig. 8 Various oil-flow images of a type IVa interaction on the 0.75-in.-radius model.

upward from this attachment point and then turn away from the leading edge. In the regions near the top and bottom of the model, away from the shock–shock interaction, the oil along the stagnation line did not move. The side oil-flow patterns show nearly horizontal streamlines flow away from the leading edge and then turn toward the slanted edges of the model. The bow shock around the model at a 0 deg AOA is a nearly normal shock, and thus the flow above the incident shock does not change direction but instead continues horizontally until the air reaches the surface of the model.

Edney [1] stated that a region of dead air exists along the leading edge below the shear layer attachment point in an oil-flow image of a 0.59-in.-radius cylinder exposed to a type IVa interaction. Although this phenomenon is not clear in the oil-flow images, the dead air region is visible in the IHEAT 1D contour maps in Figs. 9 and 10.

IHEAT 1D contour maps of the heat transfer coefficients show zoomed-out (Fig. 9) and zoomed-in (Fig. 10) views of the 0.25-, 0.50-, and 0.75-in.-radius models, from left to right, at a 0 deg AOA. A blue gap between two green regions of higher heating along the model leading edge corresponds to a valley in the heat transfer coefficients in Fig. 11. This valley may be due to the dead air zone between the lower and upper shear layer attachment points on the model. This region shrinks as the leading-edge radius increases. Either the approach Liu et al. [24] or Daryabeigi et al. [25] used to account for the effect of lateral conduction could be implemented to more accurately resolve the size of the region of influence of the impingement as the fin size increases. The green region of higher heating along the leading edge just below the dead air region on each model may be due to the flow travelling through both the incident and the bow shocks before reaching the surface of the model. The green

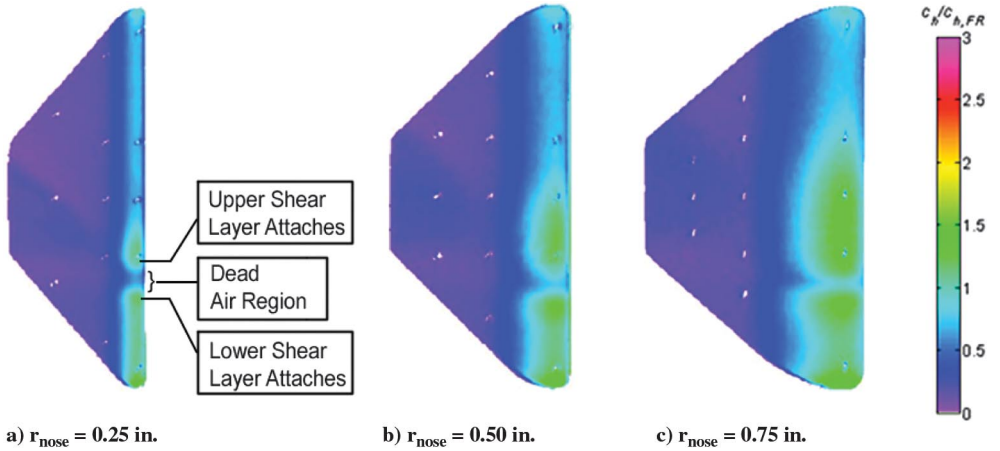

a) r_{nose} = 0.25 in. b) r_{nose} = 0.50 in. c) r_{nose} = 0.75 in.

Fig. 9 IHEAT $c_h/c_{h,FR}$ contour maps for a type IVa interaction.

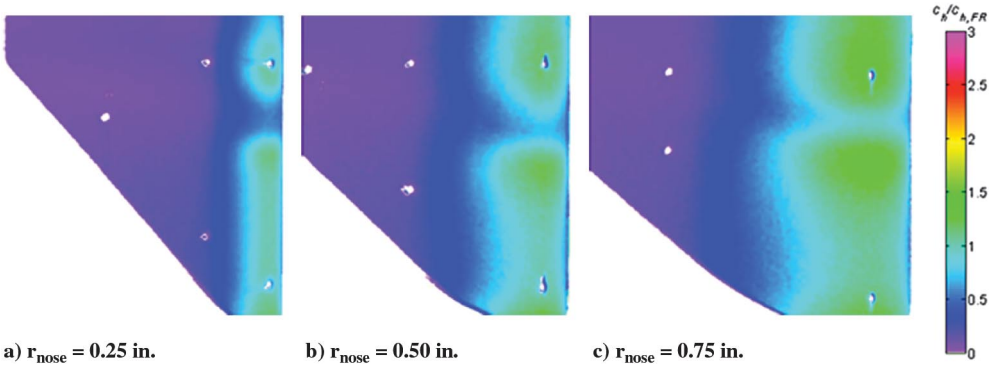

a) r_{nose} = 0.25 in. b) r_{nose} = 0.50 in. c) r_{nose} = 0.75 in.

Fig. 10 Zoomed-in IHEAT $c_h/c_{h,FR}$ contour maps for a type IVa interaction.

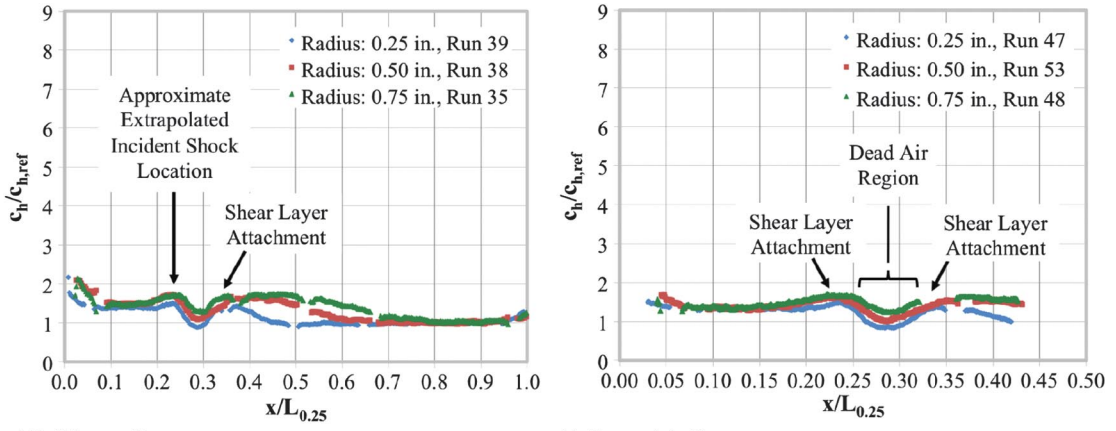

a) Full image line cut b) Zoomed-in line cut

Fig. 11 IHEAT nondimensional heat transfer coefficients for a type IVa interaction.

heating region that spans the three middle fiducials in Fig. 9c for the 0.75-in.-radius model (which shrinks with decreasing model radius) is likely due to the curved shear layer attachment above the dead air region. The increased heating at the upper and lower tips of the model is due to edge effects at the boundary between the ceramic model and the surrounding air. A repeat run was conducted for the 0.50-in.-radius model at a 0 deg AOA, and the heat transfer patterns are very similar between the two runs as expected [17].

The type IVa shock interaction yields the lowest peak heat transfer augmentation of the interactions in this study. The line cut data for all three of the model geometries display similar features for the case with a 0 deg AOA. Two small peaks of similar magnitude exist on either side of a trough in the heat transfer coefficients along the leading edge for this type of interaction. The nondimensional heat transfer data along the leading edge for the three models are presented in Fig. 11. The first peak near $x/L_{0.25} = 0.24$, with $c_h/c_{h,\text{ref}}$ approximately equal to 1.5 for the smallest model and about 1.8 for the larger models, corresponds to the lower shear layer attachment point on the leading edge near the extrapolated incident shock. Below that location on the leading edge, the heat transfer is relatively constant and elevated in each case relative to the baseline heating defined as $c_h/c_{h,\text{ref}} \approx 1$. The higher heat transfer coefficients from the lower tip of the model to the first peak are partially due to the flow passing through both the bow shock and the incident shock before contact with the surface of the model. The shear layer that forms the upper boundary of the supersonic jet attaches to the surface of the model to produce a second peak with a maximum magnitude between 1.4 for the 0.25-in.-radius model at $x/L_{0.25} = 0.36$ and 1.8 for the 0.75-in.-radius model near $x/L_{0.25} = 0.43$. The widths of the heat transfer peaks increase with increasing leading-edge radius, possibly due to conduction effects and the increased length of the shear layer before attachment. Edge effects yield increased heating at the upper and lower tips of the model for all three geometries in Fig. 9, as shown by the data for the lower tip between $x/L_{0.25} = 0$ and 0.1 in Fig. 11a. The line cut data for the two larger models are shifted to align features in the data since the model's position relative to the incident shock varied slightly with leading-edge radius.

B. Fin Sweep of −15 deg

The characteristic features of a type IV interaction are visible in the schlieren images for the 0.25-, 0.50-, and 0.75-in.-radius models (from left to right) at a −15 deg AOA in Fig. 12. One such feature is a supersonic jet emanating from the triple point that impinges nearly perpendicularly on the surface of the model. Schlieren videos of this interaction reveal changes over time in the density of the air between the bow shock and the model surface above the extrapolated incident shock location. The density gradient due to a vortex in that region is labeled in Fig. 12b but is not very clear in the still images. Although the standoff distance differs, the shape of the bow shock above and below the interaction is similar for the models with varying nose radii.

Oil-flow images for the 0.75-in.-radius model at a −15 deg AOA are provided in Fig. 13. These images display representative surface streamlines for a direct type IV shock interaction. The shear associated with the supersonic jet impingement removed the majority of the oil in that region in the full-coating images in Figs. 13b and 13d. The lower horizontal line in the two leading-edge images in this figure corresponds to the edge of this high shear region due to the supersonic jet. This line is also approximately located where the incident shock wrapped around the model (outside of the bow shock) between the two lowest fiducials on the leading edge. The lower streamlines on either side of the stagnation line in Fig. 13a resemble

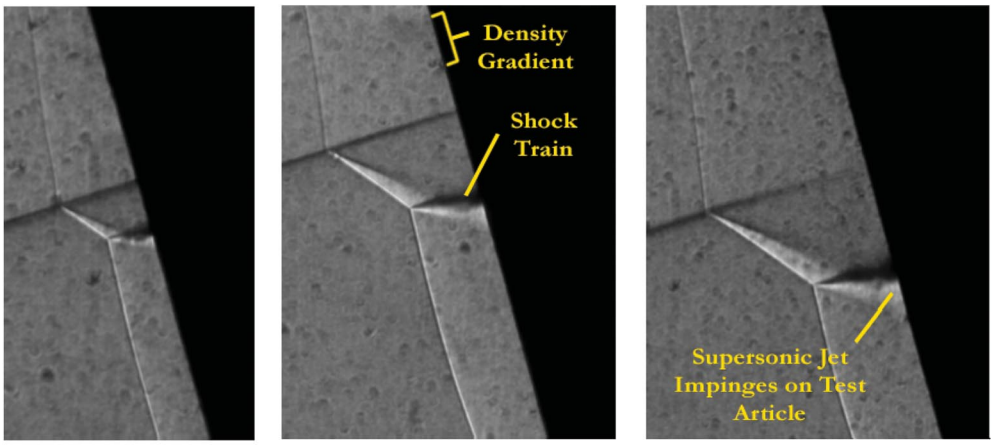

a) r_{nose} = 0.25 in. b) r_{nose} = 0.50 in. c) r_{nose} = 0.75 in.

Fig. 12 Type IV interaction zoom-schlieren images (for −15 deg AOA and a unit $Re_\infty = 2.0 \times 10^6/\text{ft}$).

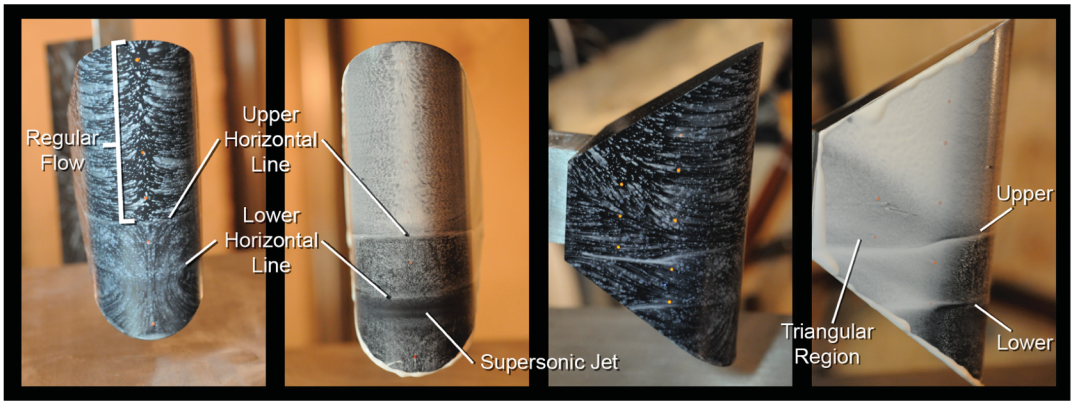

a) Dot technique b) Paint technique c) Dot technique d) Paint technique

Fig. 13 Various oil-flow images of a type IV interaction on the 0.75-in.-radius model.

parabolas with a trough centered near the supersonic jet impingement. In the corresponding schlieren images, this supersonic jet impinges on the model in a narrow horizontal region, perhaps driving the parabolic streamlines away from the leading edge.

The upper horizontal line may be due to a vortex rollup at the leading edge caused by two opposing flows meeting with the upper flow moving down and the lower flow moving up. This unsteady vortex is observed as a density fluctuation in schlieren videos. A region of stationary dots in Fig. 13a, or an undisturbed oil coating in Fig. 13b, exists along the stagnation line near the top of the leading edge. The streamlines leading away from this region above the upper horizontal line indicate flow on an inclined cylinder at Mach 6. The oil-flow images in Figs. 13c and 13d reveal side views of the same model. A triangular shape in the middle on the side of the model indicates the vortex above the extrapolated incident shock also wraps around the surface of the model. The vortex in front of the leading edge likely continues along the sidewall and then splits up into this v-shaped or triangular region.

The contour maps in Figs. 14 and 15 correspond to a type IV interaction on the 0.25-, 0.50-, and 0.75-in.-radius models, from left to right, at a −15 deg AOA. The shock interaction wraps around the model, creating streaks of higher heating coefficients on the side. A narrow peak (shown in pink with heating values either at or greater than the maximum limit on the color bar) on the leading edge corresponds to the supersonic jet impingement point. This peak region widens as the leading-edge radius increases. The higher heating regions above and below the peak region also spread farther parallel to (and around the circumference of) the leading edge as the radius increases.

The direct type IV shock–shock interaction produces a sharp, narrow peak heat transfer augmentation as shown in Fig. 16. Peak values were derived from the zoomed-in data for this case since the few data points in the zoomed-out peak region for the 0.25-in.-radius model exceeded the phosphor limit by the time $t = 1.8$ s. The peak has a maximum magnitude of 4.6 for the smallest model and about 6.8 for the largest model located at approximately $x/L_{0.25} = 0.24$. The width of the peak region ranges from approximately 0.025 nondimensionally (or 0.1 in.) to 0.06 (or 0.24 in.). Two small peaks exist on either side of the peak heat transfer coefficient for the smallest model. The unsteady vortex above the incident shock, likely combined with lateral conduction effects, yields a region of increased heating bounded by the upper and lower marks in Fig. 14c with either a smaller peak of about 1.5 for the smallest model or a broader peak of about $c_h/c_{h,\mathrm{ref}} = 2$ for the larger models.

Since the flow that contacts the model surface between $x/L_{0.25} = 0$ and 0.2 passes through both the incident shock and the bow shock, the heat transfer coefficients below the major peak along the leading edge of the model exceed the baseline value with a small plateau of heat transfer coefficients between 2.3 and 2.9. The increased heating at the upper tip of the model is evident in Fig. 16a. The shock–shock interaction moves down the leading edge as the radius of the model increases, affecting the heat transfer to the lower tip of the model. The heat transfer coefficient contours near the lowest fiducial on the leading-edge change from green to yellow and orange with increasing model radius. The shorter the distance between the peak and the edge of the model is, the greater the heat flux is in that region due to the conduction from the peak down the length of the model.

C. Fin Sweep of −25 deg

Figure 17 shows schlieren images (from left to right) of a type III interaction for the 0.25-, 0.50-, and 0.75-in.-radius models at a −25 deg AOA. In the type III interaction, the supersonic jet of the previous two interaction types is replaced with a shear layer that attaches to the surface of the model. Supersonic flow exists in the triangular region between the turned bow shock and the shear layer in the image [1]. Although the shear layer attachment point is not clearly evident in the zoom-schlieren images, the shear layer leaves the triple

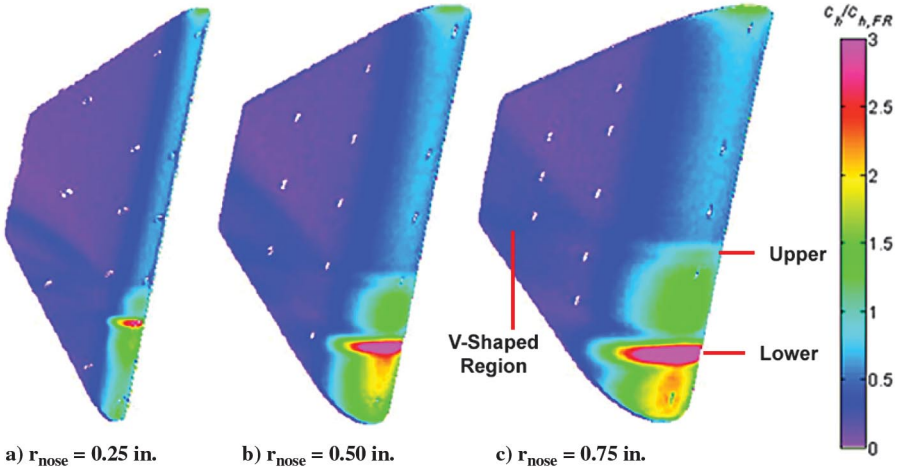

a) r_{nose} = 0.25 in. b) r_{nose} = 0.50 in. c) r_{nose} = 0.75 in.

Fig. 14 IHEAT $c_h/c_{h,\mathrm{FR}}$ contour maps for a type IV interaction.

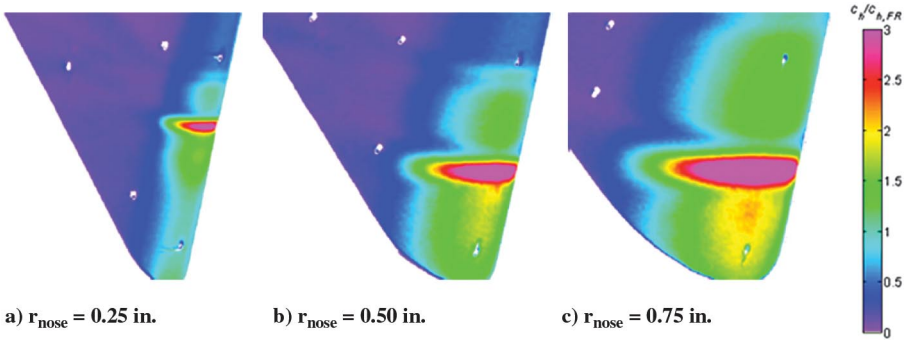

a) r_{nose} = 0.25 in. b) r_{nose} = 0.50 in. c) r_{nose} = 0.75 in.

Fig. 15 Zoomed-in IHEAT $c_h/c_{h,\mathrm{FR}}$ contour maps for a type IV interaction.

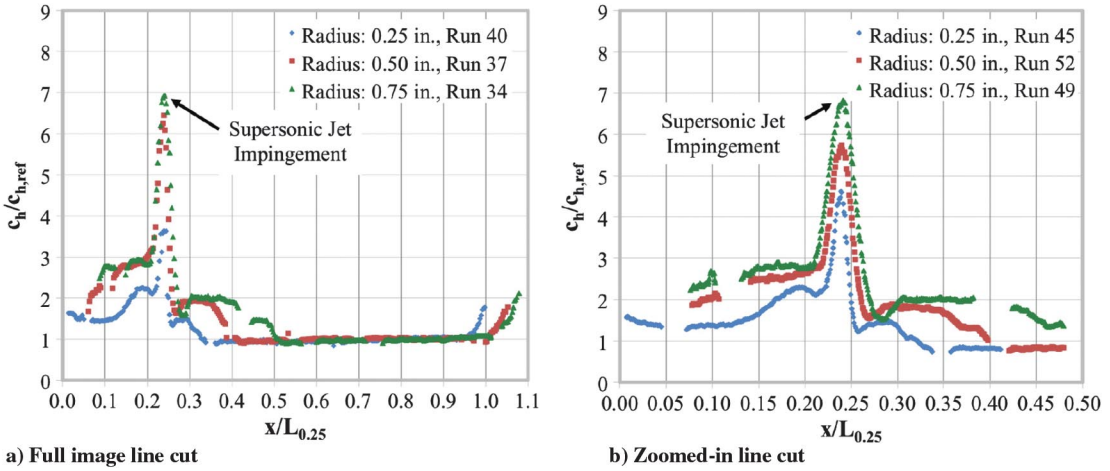

a) Full image line cut b) Zoomed-in line cut

Fig. 16 IHEAT nondimensional heat transfer coefficients for a type IV interaction.

point with the incident and bow shocks at the appropriate angle to connect to the model surface at the same location as the reflected shock. An unsteady region between the model surface and the shear layer near the attachment point is labeled as a density gradient in Fig. 17b. This phenomenon is clearer in schlieren videos of the interaction for the three geometries and contributes to the difficulty in capturing the shear layer attachment in a still image. As with the −15 deg AOA case, the interaction impingement point moves down the leading edge of the model as the leading-edge radius increases.

The type III shock–shock interaction mainly affects the leading-edge streamlines near the extreme lower tip of the model as shown in Fig. 18 for the 0.75-in.-radius model. The streamline behavior for this model was similar to the patterns observed on the 0.25- and 0.50-in.-radius models, although the shock-interaction region occurred higher on the leading edge in those cases. The pattern in the interaction region also resembles the oil-flow streamlines obtained for a type III interaction for a 1.18-in.-wide flat plate in [1]. As in the −15 deg AOA oil-flow images, the streamlines near the top of the leading edge in both images follow a curved path down and away from the stagnation region. The streamlines for a −25 deg AoA move farther downward than for the −15 deg case, as expected, since the bow shock is angled farther forward and the flow crossing the shock turns down at a sharper angle.

The shock-interaction region produces a stagnation region below the shear layer attachment point from which the streamlines on the leading edge fan out as shown in the image in Fig. 18a obtained using

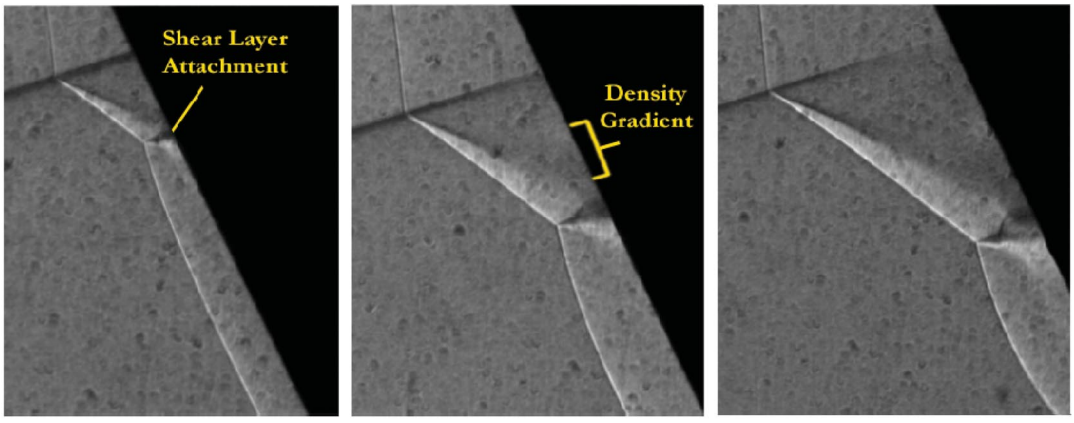

a) r_{nose} = 0.25 in. b) r_{nose} = 0.50 in. c) r_{nose} = 0.75 in.

Fig. 17 Type III interaction zoom-schlieren images (for −25 deg AOA and a unit $Re_\infty = 2.0 \times 10^6$/ft).

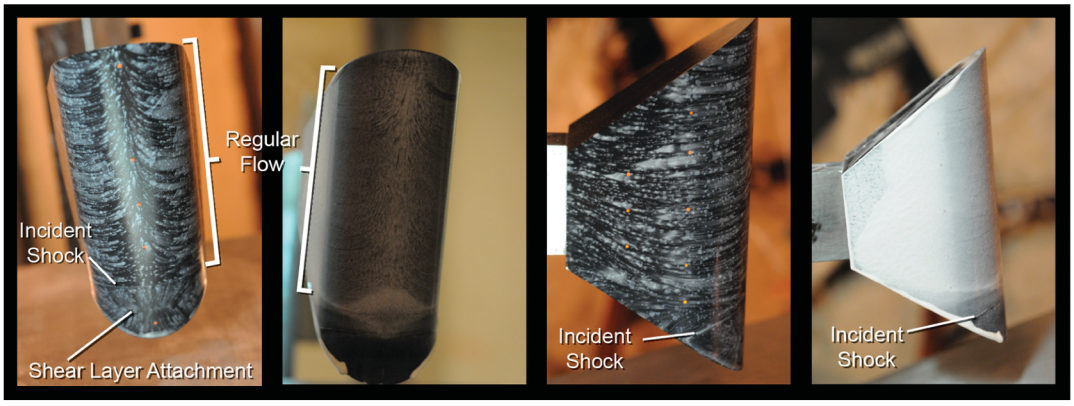

a) Dot technique b) Paint technique c) Dot technique d) Paint technique

Fig. 18 Various oil-flow images for a type III interaction on the 0.75-in.-radius model.

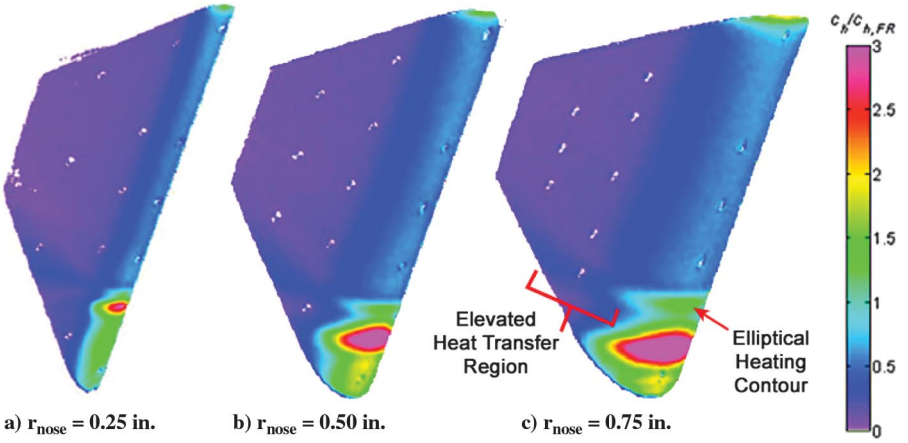

Fig. 19 IHEAT $c_h/c_{h,\mathrm{FR}}$ contour maps for a type III interaction.

dots of oil. The motion of the flow above and below the shear layer impingement location as demonstrated in the zoom-schlieren data agrees with the orientation of these streamlines. The oil-flow images in Figs. 18c and 18d were captured at an angle rather than horizontally. Thus, the line wrapping around the images near the extrapolated incident shock location appears to be angled downward but instead should be roughly horizontal.

A type III shock–shock interaction produces a broader peak heat transfer. Contour maps for the 0.25-, 0.50-, and 0.75-in.-radius models (from left to right) at a −25 deg AOA are included in Figs. 19 and 20. The effects of the shock interaction wrap around the model, creating streaks of higher heating. Again, the width of the peak heat transfer region increases laterally and circumferentially with increasing leading-edge radius. The extrapolated incident shock location is near a green elliptical contour above the main peak that leads to a narrow region of higher heat transfer values on the side of the model. This ellipse of elevated heating is likely due to the density gradient below the incident shock in the schlieren images and videos, which may be caused by the stagnation of the opposing streamlines along the leading edge. Videos generated from numerical schlieren images in [17] demonstrate the flow due to the attaching shear layer moves up and the flow passing through the bow shock above the interaction moves down.

The zoomed-in plot in Fig. 21 shows a peak at the shear layer attachment point (at $x/L_{0.25} = 0.22$) with a width of 0.065 (0.26 in.) and a maximum value of at least 5.2 for the 0.25-in.-radius model. Again, the actual peak was not calculated for the zoomed-out line cut in this case since the maximum temperature exceeds the phosphor limit of about 320 °F at $t = 1.8$ s. Both the width and the maximum value of the peak due to the shear layer attachment point increases to

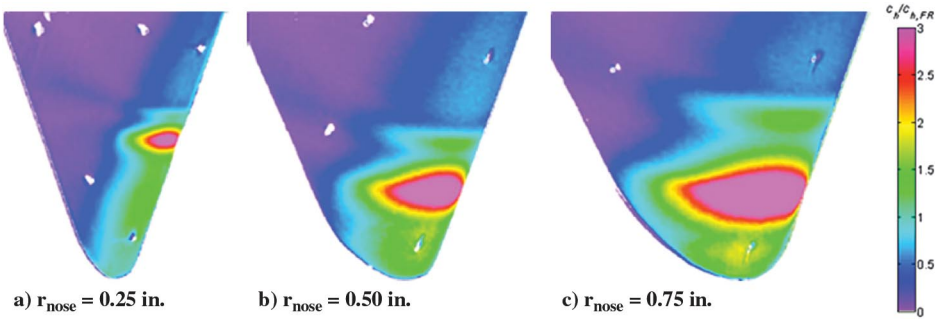

Fig. 20 Zoomed-in IHEAT $c_h/c_{h,\mathrm{FR}}$ contour maps for a type III interaction.

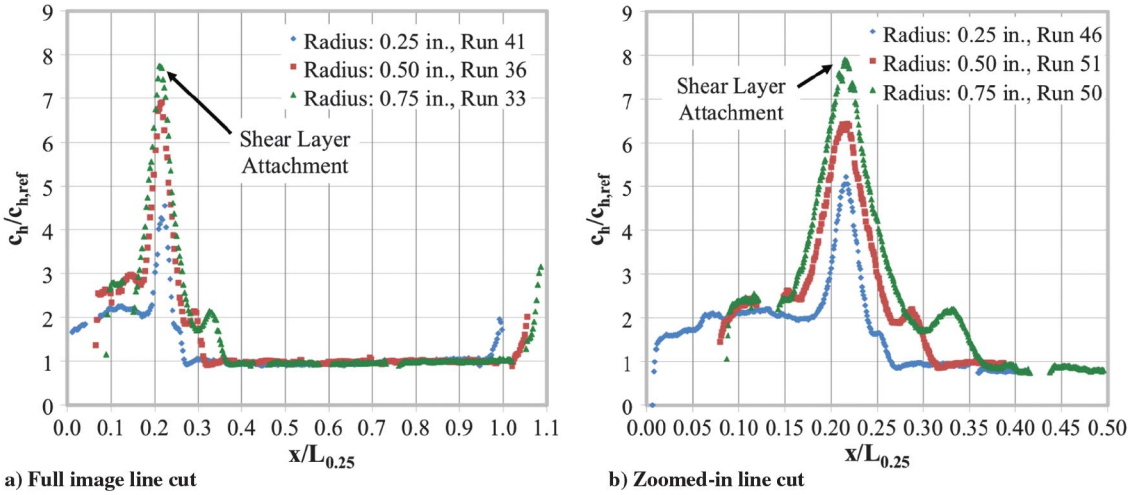

Fig. 21 IHEAT nondimensional heat transfer coefficients for a type III interaction.

0.14 nondimensionally (or 0.55 in.) and 7.9, respectively, for the 0.75-in.-radius model.

The heat transfer to the lower portion of the leading edge is about twice the baseline heating for the smallest model and higher for the larger models. Warmer air that passes through the bow and incident shock may be partially responsible for this heating, as well as conduction through the model and the proximity of the higher peak relative to the tip of the model. The angle of the shear layer relative to the incident shock for a type III interaction varies by a few degrees between the three model geometries. Therefore, the shear layer attachment point moves down the leading edge as the bow shock standoff distance increases and produces a greater distance between the triple point and the surface of the model. Therefore, the region of peak heating moves closer to the lowest fiducial mark as the leading-edge radius increases for a type III interaction, as expected from the zoom-schlieren images. The line cuts in Fig. 21 are translated to align the heating peaks for the different models.

Additional information about the magnitude and location of the peaks and valleys in the line cuts is in [17]. For example, a unit Re_∞ number sweep was conducted to determine the impact of the unit Re_∞ number on the peak heating due to the type IV interaction. Also, 1D FV data are provided in [17] to compare to the IHEAT results.

1. *1D vs 2D Heat Transfer*

Temperature data obtained in a run with a flow unit Re_∞ number of 1.1×10^6/ft were used to compute leading-edge heat transfer coefficients to provide a comparison between 1D and 2D heat transfer analyses. The plots in Figs. 22 and 23 show enthalpy-based dimensional and nondimensional heat transfer coefficients along the leading edge of a 0.25-in.-radius model at a −15 deg AOA. The input data to the FV codes for this run were changed from every frame to every sixth frame (0.2 s apart) of the recorded surface temperature data obtained during Run 43. The radial spacing is $\Delta r = 2.5 \times 10^{-4}$ in. between nodes. Data were extracted from 358 pixels along the leading edge, so the lateral spacing is $\Delta z = 1.12 \times 10^{-2}$ in. between nodes.

The maximum value of the y axis of the dimensional plot in Fig. 22 is 0.40 and in Fig. 23 is 0.30 since these two plots show coefficients in units of $\mathrm{lb}_m/(\mathrm{ft}^2 \cdot \mathrm{s})$. The limits on the x axis are also changed to $x/L = 0.1$ to 0.5 for the plots in these two figures to better show the differences between the 1D and 2D line cut data. The full line cuts for these comparisons are presented in [17]. The peak heating augmentation due to the supersonic jet impingement is narrower and higher for the 2D case than for the 1D cases. For the dimensional line cuts in Fig. 22, at $t = 3.4$ s into the run, the 2D FV peak heat transfer is about 16% greater than the peak value from IHEAT. The 2D FV nondimensional peak heat transfer coefficient is approximately 38% higher than the corresponding IHEAT peak value.

The dimensional heat transfer coefficients derived using a 2D method in the region away from the shock–shock interaction region on the leading edge are lower than those calculated by either 1D method. This trend is correct since the 2D code accounts for lateral conduction, thereby reducing the heat assumed to travel in the radial direction because heat also moves to either side of the cell in the lateral direction. The nondimensional coefficients away from the peak collapse on top of each other, suggesting the offset from the IHEAT output due to the 1D and 2D FV methods is uniform in those regions.

In the dimensional plot in Fig. 23, the 2D peak heat transfer is about 20% greater than the IHEAT result. As expected, the difference between the IHEAT and 2D outputs increases later in the run due to errors

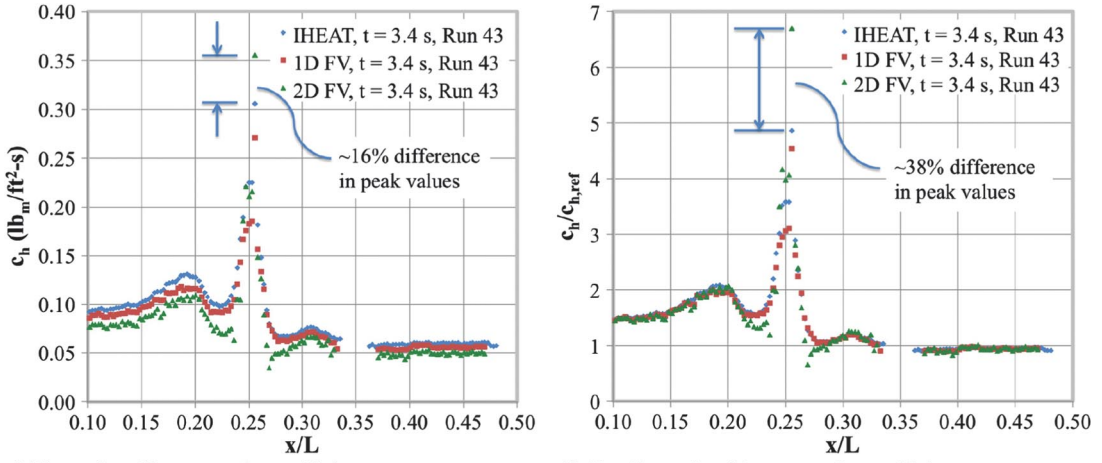

a) Dimensional heat transfer coefficients b) Nondimensional heat transfer coefficients

Fig. 22 Type IV interaction heat transfer coefficients for a unit $Re_\infty = 1.1 \times 10^6$/ft (at $t = 3.4$ s).

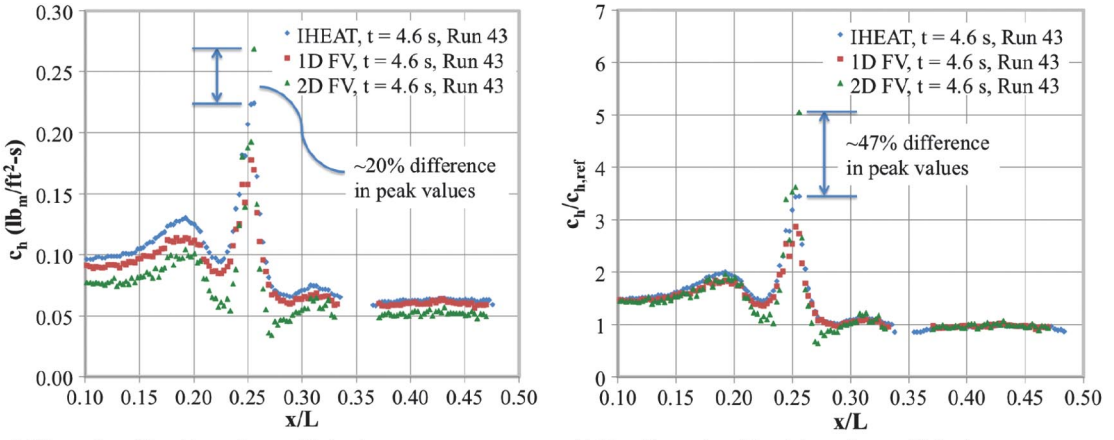

a) Dimensional heat transfer coefficients b) Nondimensional heat transfer coefficients

Fig. 23 Type IV interaction heat transfer coefficients for a unit $Re_\infty = 1.1 \times 10^6$/ft (at $t = 4.6$ s).

associated with neglecting the lateral conduction and the semi-infinite assumption in IHEAT. Again, the difference between the heat transfer peaks for the 2D and IHEAT codes increases when the heat transfer coefficients are divided by a reference value to yield nondimensional data. In the nondimensional plot, the 2D FV peak heat transfer augmentation is about 47% higher than the IHEAT peak value. Berry and Nowak [11] predicted a nondimensional peak heating augmentation in the type IV interaction produced by a −15 deg AOA for a unit $Re_\infty = 2.1 \times 10^6$/ft would increase 43%, from about 7 to 10, if lateral conduction effects were considered in the heat transfer analysis.

Temperature data also are available along the entire leading edge near the end of the wind tunnel runs for the lower heating cases. Thus, the 2D FV code was implemented using the temperature data at $t = 4.6$ s for the 0.75-in.-radius model at a 0 deg AOA to compare to the 1D IHEAT results. This comparison is shown for nondimensional heat transfer coefficients in Fig. 24. The greatest difference between the 1D and 2D results is at the valley between the extrapolated incident shock location and the shear layer attachment points. In the nondimensional heat transfer coefficients, the 2D FV value for the minimum heat transfer coefficient in this valley is about 12% lower than the minimum IHEAT value. The nondimensional 1D and 2D heat transfer coefficients are similar away from the valley.

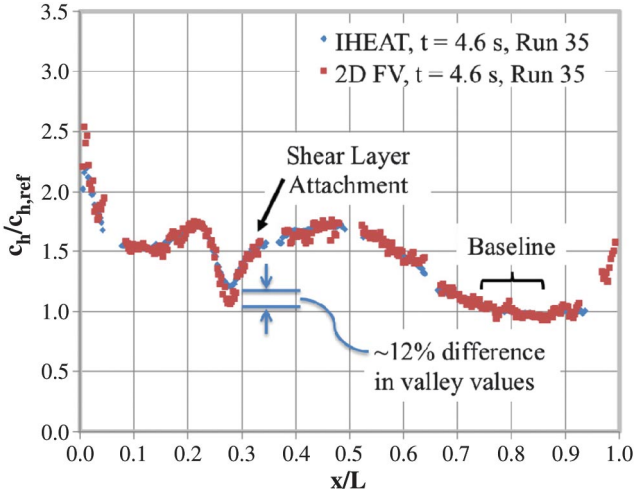

Fig. 24 Type IVa interaction nondimensional heat transfer coefficients for a unit $Re_\infty = 2.1 \times 10^6$/ft.

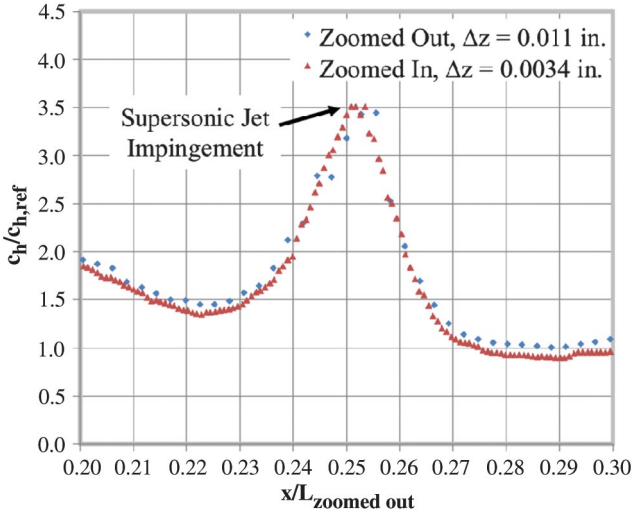

Fig. 25 Spatial resolution of IHEAT nondimensional heat transfer coefficients for a type IV interaction.

2. Spatial Resolution

Separate runs were conducted for each model configuration with the phosphor camera either zoomed out to capture the full side and leading edge of the model or zoomed in to view only the areas near the shock–shock interaction. The plot in Fig. 25 shows a comparison of the peak region between the nondimensional heat transfer coefficients for the zoomed-in and zoomed-out runs with a −15 deg AOA and a unit $Re_\infty = 1.1 \times 10^6$/ft. The x axis positions for the zoomed-in data are shifted by a small amount to align the peak location between the two runs.

The spatial resolution of the zoomed-in data is about 3.8 times greater than the resolution for the zoomed-out heat transfer data. The spatial resolution of the phosphor data ranges from 0.0105 to 0.015 in. between the acquired temperatures for the zoomed-out cases, and the resolution is about 0.004 in. for the zoomed-in cases (or 0.0034 in. for the configuration in Fig. 25). These spatial resolutions are sufficient for the heat transfer experiments and confirm the minimum thin-film-gauge spacing of 0.015 in. found in [11] deemed necessary to capture the narrow heating spike for type III and type IV interactions accurately. Thus, the increased resolution of the zoomed-in data provides additional confidence that the observed trends in the zoomed-out data properly represent the heat transfer behavior for each shock–shock interaction.

VI. Conclusions

The type IVa [0 deg angle of attack (AOA)], direct type IV (−15 deg AOA), and type III (−25 deg AOA) shock–shock interactions were investigated using three model geometries with leading-edge radii of 0.25, 0.50, and 0.75 in., respectively. Flow density gradients were observed using a zoom-schlieren technique, and the surface flow was visualized using oil-flow methods. The general heating behaviors for these three interactions were assessed using one-dimensional (1D) Imaging for Hypersonic Experimental Aeroheating Testing (IHEAT) contour maps. The leading-edge heat transfer coefficients were analyzed for each run using 1D semi-infinite and finite-volume methods. A two-dimensional (2D) finite-volume method also was used to analyze the heat transfer behavior for two cases.

Previous studies suggest a greater spatial resolution than 0.015 in. between gauges is necessary to experimentally resolve the heat transfer peak for the type IV interaction. The spatial resolution of the phosphor thermography data ranged from 0.004 to 0.015 in. Therefore, the data resolution was better than or comparable to the discrete temperature gauge spacing on models used in previous shock–shock interaction studies. This improved spatial resolution is significant because the heat transfer data from these line cuts displayed similar trends to equivalent cases in the literature. Thus, 0.015 in. gauge spacing is sufficient to accurately capture the narrow peak heat transfer augmentation due to a type III or type IV interaction. The zoomed-in line cut data yielded lower than expected results for the nondimensional peak heat transfer data in several cases, likely due to the limitation on the reference values used to convert the heat transfer data for these runs to nondimensional values.

Based on these observations, the type IVa shock–shock interaction exhibited the smallest peak heating augmentation. The type IV interaction produced a narrow, steep heat transfer peak due to an impinging supersonic jet. The type III interaction did not include a supersonic jet as in the other two cases but instead yielded a broader peak in the heat transfer coefficients at the shear layer attachment point. Qualitatively, the heat transfer profiles from this study are similar to the corresponding type III and type IV cases in a prior study.

The nondimensional peak heat transfer for a given type of shock–shock interaction increases as the leading-edge radius increases, and the dimensional heat transfer coefficients follow the opposite trend. As the leading-edge radius increases, the baseline heat transfer coefficients away from the shock–shock interaction region decrease. This trend yields a lower averaged reference value for the larger models, which amplifies the nondimensional peak heat transfer augmentation compared to the smaller model geometries.

Dimensionally, the peak heat transfer coefficient from a 2D finite-volume analysis was approximately 20% higher than the result from a 1D semi-infinite analysis for a type IV interaction, which corroborates previous findings for a similar shock–shock interaction case. The nondimensional peak heat transfer augmentation calculated for a type IV interaction at a unit $Re_\infty = 1.1 \times 10^6/\text{ft}$ using a 2D alternating direction implicit method was about 47% higher than the value predicted using the 1D semi-infinite IHEAT code at a time 4.6 s into the run. This difference between 1D and 2D heat transfer results is a reasonable estimate if predicted augmentation for a unit $Re_\infty = 1.1 \times 10^6/\text{ft}$ case can be extrapolated to a unit $Re_\infty = 2.1 \times 10^6/\text{ft}$ case. For the type IVa interaction with smaller temperature gradients in the lateral direction, the difference between the 1D and 2D heat transfer results was likewise smaller. Thus, a multidimensional conduction analysis is necessary to account for lateral conduction in cases with large temperature gradients.

Acknowledgments

The authors would like to thank Kamran Daryabeigi for his help in writing and debugging the finite-volume conduction codes used in this study. The authors also thank Elaine Scott, Michael von Spakovsky, Walter O'Brien, and Shann Rufer for their assistance in this research.

References

[1] Edney, B., "Anomalous Heat Transfer and Pressure Distributions on Blunt Bodies at Hypersonic Speeds in the Presence of an Impinging Shock," Aeronautical Research Inst. of Sweden, FFA Rept. 115, Stockholm, 1968.

[2] Andreadis, D., *Scramjet Engines Enabling the Seamless Integration of Air and Space Operations*, Pratt and Whitney, West Palm Beach, FL, 2004.

[3] Harwood, W., "Board Hearing Shows Work to Piece Together Known Data," Spaceflight Now, Inc., http://www.spaceflightnow.com/shuttle/sts107/030318hearing/ [retrieved 01 March 2013].

[4] Watts, J. D., "Flight Experiment with Shock Impingement and Interference Heating on the X-15-2 Research Airplane," NASA TM-X-1669, 1968.

[5] Keyes, J. W., and Hains, F. D., "Analytical and Experimental Studies of Shock Interference Heating in Hypersonic Flows," NASA TN-D-7139, May 1973.

[6] Nowak, R., Holden, M., and Wieting, A., "Shock/Shock Interference on a Transpiration Cooled Hemispherical Model," AIAA Paper 1990-1643, June 1990.

[7] Bushnell, D. M., "Interference Heating on a Swept Cylinder in Region of Intersection with a Wedge at Mach Number 8," NASA TN-D-3094, 1965.

[8] Bushnell, D. M., "Effects of Shock Impingement and Other Factors on Leading-Edge Heat Transfer," NASA TN-D-4543, April 1968.

[9] Carter, H. S., and Carr, R. E., "Free-Flight Investigation of Heat Transfer to an Unswept Cylinder Subjected to an Incident Shock and Flow Interference from an Upstream Body at Mach Numbers up to 5.50," NASA TN-D-988, 1961.

[10] Hiers, R. S., and Loubsky, W. J., "Effects of Shock-Wave Impingement on the Heat Transfer on a Cylindrical Leading Edge," NASA TN-D-3859, 1967.

[11] Berry, S. A., and Nowak, R. J., "Fin Leading-Edge Sweep Effect on Shock-Shock Interaction at Mach 6," *Journal of Spacecraft and Rockets*, Vol. 34, No. 4, July–Aug. 1997, pp. 416–425. doi:10.2514/2.3247

[12] Wright, M. J., Nowak, R. J., Berry, S. A., Glass, C. E., and Candler, G. V., "Numerical/Experimental Investigation of 3-D Swept Fin Shock Interactions," AIAA Paper 1998-2816, June 1998.

[13] Walker, D. G., and Scott, E. P., "The Effects of Lateral Conduction on Heat Flux Estimation from Surface Temperature Measurements," *Proceedings of the Seventh AIAA/American Society of Mechanical Engineers Joint Thermophysics and Heat Transfer Conference*, Vol. 3, Albuquerque, NM, June 1998, pp. 245–252.

[14] Berger, K. T., Hollingsworth, K. E., Wright, S. A., and Rufer, S. J., "NASA Langley Aerothermodynamics Laboratory: Hypersonic Testing Capabilities," AIAA Paper 2015-1337, Jan. 2015.

[15] Rhode, M. N., and DeLoach, R., "Hypersonic Wind Tunnel Calibration Using the Modern Design of Experiments," AIAA Paper 2005-4274, July 2005.

[16] Hollis, B. R., and Collier, A. S., "Turbulent Aeroheating Testing of Mars Science Laboratory Entry Vehicle," *Journal of Spacecraft and Rockets*, Vol. 45, No. 3, 2008, pp. 417–427. doi:10.2514/1.31798

[17] Jones, M. L., "Experimental Investigation of Shock-Shock Interactions over a 2-D Wedge at $M = 6$," Master's Thesis, Virginia Polytechnic Inst. and State Univ., Hampton, VA, 2013.

[18] Buck, G. M., Powers, M. A., Griffith, M. S., Hopkins, J. W., Veneris, P. H., and Kuykendoll, K. A., "Fabrication of 0.0075-Scale Orbiter Phosphor Thermography Test Models for Shuttle RTF Aeroheating Studies," NASA TM-2006-214507, Nov. 2006.

[19] Merski, N. R., "Reduction and Analysis of Phosphor Thermography Data with the IHEAT Software Package," AIAA Paper 1998-0712, Jan. 1998.

[20] Merski, N. R., "Global Aeroheating Wind-Tunnel Measurements Using Improved Two-Color Phosphor Thermography Method," *Journal of Spacecraft and Rockets*, Vol. 36, No. 2, 1999, pp. 160–170. doi:10.2514/2.3446

[21] Burden, R. L., and Faires, J. D., "Crank-Nicolson Algorithm," *Numerical Analysis*, 8th ed., Thomson Brooks/Cole, Belmont, CA, 2005, pp. 707–709.

[22] Tannehill, J. C., Anderson, D. A., and Pletcher, R. H., "Thomas and Alternating Direction Implicit Algorithms," *Computational Fluid Mechanics and Heat Transfer*, 2nd ed., Taylor and Francis, Philadelphia, PA, 1997, pp. 114, 115, 139–142, 151, 152.

[23] Fay, J. A., and Riddell, F. R., "Theory of Stagnation Point Heat Transfer in Dissociated Air," *Journal of the Aeronautical Sciences*, Vol. 25, No. 2, Feb. 1958, pp. 73–85, 121.

[24] Liu, T., Wang, B., Sullivan, J., and John, P., "Correcting Lateral Heat Conduction Effect in Image-Based Heat Flux Measurements as an Inverse Problem," *International Journal of Heat and Mass Transfer*, Vol. 54, Nos. 5–6, 2011, pp. 1244–1258.

[25] Daryabeigi, K., Berry, S. A., Horvath, T. J., and Nowak, R. J., "Finite Volume Numerical Methods for Aeroheating Rate Calculations from Infrared Thermographic Data," *Journal of Spacecraft and Rockets*, Vol. 43, No. 1, 2006, pp. 54–62. doi:10.2514/1.14500

R. Kimmel
Associate Editor